



Phase transitions and domain structures of ferroelectric nanoparticles: Phase field model incorporating strong elastic and dielectric inhomogeneity

J.J. Wang^{a,*}, X.Q. Ma^a, Q. Li^b, J. Britson^c, Long-Qing Chen^{c,d}

^a Department of Physics, University of Science and Technology Beijing, Beijing 100083, People's Republic of China

^b State Key Laboratory for Strength and Vibration, School of Aerospace, Xi'an Jiaotong University, Xian 710049, People's Republic of China

^c Department of Materials Science and Engineering, The Pennsylvania State University, University Park, PA 16802, USA

^d State Key Laboratory of New Ceramics and Fine Processing, School of Materials Science and Engineering, Tsinghua University, Beijing 100084, People's Republic of China

Received 11 May 2013; received in revised form 9 August 2013; accepted 27 August 2013

Available online 1 October 2013

Abstract

An efficient numerical algorithm based on a Fourier spectral iterative perturbation method is proposed to accurately compute the electrostatic fields in three-dimensional (3D) microstructures with arbitrary dielectric inhomogeneity and anisotropy. The method can be conveniently implemented in phase field modeling of microstructure evolution in systems with inhomogeneous dielectric constants as well as inhomogeneous polarization and charge distributions. It is employed to determine the temperature–shape (aspect ratio) phase diagram, domain structures, and domain switching of PbTiO_3 nanoparticles using phase field simulations. It is shown that the Curie temperature is enhanced for nanowires and nanorods and reduced for nanodots. The critical sizes below which the ferroelectricity disappears for the nanowire and thin film are estimated to be around 1.4 nm. Vortex domain structures are found in nanorods, nanodots, and nanodisks. Results are in general agreement with existing experimental observations and first principle calculations. Crown Copyright © 2013 Published by Elsevier Ltd. on behalf of Acta Materialia Inc. All rights reserved.

Keywords: Dielectric inhomogeneity; Ferroelectric nanoparticle; Phase field method; Ferroelectric phase transitions

1. Introduction

Nanoscale ferroelectrics have received considerable attention due to their potential applications in microelectronics [1], such as non-volatile ferroelectric random access memory (NFERAM) [2]. For example, ferroelectric nanowires (FNWs) are being considered as a new medium for next generation ultrahigh density computer memory [3–5]. Many ferroelectric nanostructures of controlled size and shape have been synthesized [6–12]. Mao et al. synthesized single crystalline BaTiO_3 nanowires using a simple

one step solid-state chemical reaction [10]. Urban et al. showed that crystalline nanorods composed of BaTiO_3 and SrTiO_3 with a cubic perovskite structure could be synthesized by solution-based decomposition of bimetallic alkoxide precursors [7].

The size and shape of a ferroelectric device strongly affect the Curie temperature and polarization morphologies, and extensive experimental and theoretical studies have been carried out to investigate the phase transitions in nanoscale ferroelectric particles. For example, Spanier et al. used scanning probe microscopy to measure the ferroelectric phase transition temperatures in individual BaTiO_3 nanowires and obtained diameter-dependent Curie temperatures [12]. Naumov et al. investigated free-standing nanoparticles of perovskite $\text{Pb}(\text{Zr}_{0.5}\text{Ti}_{0.5})\text{O}_3$ (PZT) with disk and rod shapes

* Corresponding author.

E-mail address: wjj8384@gmail.com (J.J. Wang).

using ab initio calculations. They found that vortex domain structures are stable in these nanoparticles [5]. Moreover, assuming polarization is along the axial direction (x_3 direction of the coordinate plane) of the nanoparticles, Morozovska et al. used the direct variational method to solve the Euler–Lagrange equations derived from the Landau–Ginzburg–Devonshire (LGD) free energy expression to obtain an approximate analytical expression for the dependence of Curie temperature on the size, polarization gradient coefficient, extrapolation length, effective surface tension, and electrostriction coefficient [13]. Ignoring surface tension and assuming a homogeneous polarization distribution in epitaxial BaTiO₃ nanowires Wang et al. studied the strain effects on the phase transition of BaTiO₃ nanowires using Landau theory [14].

Modeling the phase transitions and domain structures of ferroelectric nanoparticles requires solutions to the Poisson equation in an electrically inhomogeneous and anisotropic system with spatially dependent dielectric constants, electric polarization, and charge density distributions. Solving the electrostatic equilibrium equation in an inhomogeneous system is also a common problem in modeling many other materials, including batteries, solid oxide fuel cells, dielectric capacitors, and dielectric/ferroelectric heterostructures, such as ferroelectric superlattices, ferroelectric islands, ferroelectric polycrystals, and epitaxially grown ferroelectric thin films or nanowires, and ferroelectrics with voids/cracks.

In order to solve the elastic equilibrium equation with arbitrary elastic inhomogeneity and anisotropy a number of numerical algorithms have been proposed. These include the conjugate gradient method (CGM) [15,16], phase field microelasticity method (PFMM) [17,18], Fourier spectral iterative perturbation method (SPM) [19], as well as a combination of the uniform eigenstrain method (UEA) and the Fourier iterative spectral perturbation method (SPM) [20]. The similarity of the electrostatic equilibrium equation to the mechanical equilibrium equation motivated us to develop an SPM to solve the electrostatic equilibrium equation for systems with arbitrary electric inhomogeneity and anisotropy.

As an example, we studied the shape and size effects on the phase transitions and domain structures of ferroelectric nanoparticles. In Section 2 we outline the Fourier iterative SPM for calculating the electric potential and electric field for systems with arbitrary electric inhomogeneity and anisotropy. In Section 3 we describe a phase field model for simulating the ferroelectric nanoparticles. The results and discussion are given in Section 4. The paper concludes with a short summary.

2. Solution of the electric equilibrium equation

Here we give a general description of an electrically inhomogeneous system and then solve the electrical equilibrium equations by the SPM scheme. The dielectric constant is spatially dependent and anisotropic. The

position-dependent total polarization $\mathbf{P}^T(\mathbf{r}, \mathbf{E})$ for dielectrics/ferroelectrics as a function of the electric field \mathbf{E} can be written as

$$\mathbf{P}^T(\mathbf{r}, \mathbf{E}) = \mathbf{P}^S(\mathbf{r}) + \mathbf{P}^E(\mathbf{r}, \mathbf{E}), \quad (2.1)$$

where $\mathbf{P}^S(\mathbf{r})$ is the spontaneous polarization and $\mathbf{P}^E(\mathbf{r}, \mathbf{E})$ is the polarization induced by the electric field $\mathbf{E}(\mathbf{r})$. In general the induced polarization and local electric field are related by the equation

$$\mathbf{P}^E(\mathbf{r}, \mathbf{E}) = \varepsilon_0 \boldsymbol{\chi}(\mathbf{r}, \mathbf{E}) \cdot \mathbf{E}, \quad (2.2)$$

where ε_0 is the vacuum dielectric constant and $\boldsymbol{\chi}(\mathbf{r}, \mathbf{E})$ is the field-dependent dielectric permittivity of the reference crystal far from any lattice instability [21–23]. In this work $\boldsymbol{\chi}(\mathbf{r})$ is assumed to be \mathbf{E} -independent. Thus, the induced $\mathbf{P}^E(\mathbf{r}, \mathbf{E})$ is written as

$$\mathbf{P}^E(\mathbf{r}, \mathbf{E}) = \varepsilon_0 \boldsymbol{\chi}(\mathbf{r}) \mathbf{E}(\mathbf{r}). \quad (2.3)$$

The total electric field $\mathbf{E}(\mathbf{r})$ originates from the external electric field \mathbf{E}^{ext} and the depolarization field $\mathbf{E}^d(\mathbf{r})$, caused by the spontaneous polarization $\mathbf{P}^S(\mathbf{r})$, i.e.

$$\mathbf{E}(\mathbf{r}) = \mathbf{E}^{\text{ext}} + \mathbf{E}^d(\mathbf{r}). \quad (2.4)$$

Therefore the electric displacement $\mathbf{D}(\mathbf{r}, \mathbf{E})$ can be written either in terms of total polarization $\mathbf{P}^T(\mathbf{r}, \mathbf{E})$ or spontaneous polarization $\mathbf{P}^S(\mathbf{r})$ by substituting Eqs. (2.2) and (2.3) into the electric displacement expression, i.e.

$$\begin{aligned} \mathbf{D}(\mathbf{r}, \mathbf{E}) &= \varepsilon_0 \mathbf{E}(\mathbf{r}) + \mathbf{P}^T(\mathbf{r}, \mathbf{E}) \\ &= \varepsilon_0 \mathbf{E}(\mathbf{r}) + \mathbf{P}^S(\mathbf{r}) + \varepsilon_0 \boldsymbol{\chi}(\mathbf{r}) \mathbf{E}(\mathbf{r}) \\ &= \varepsilon_0 \boldsymbol{\kappa}(\mathbf{r}) \mathbf{E}(\mathbf{r}) + \mathbf{P}^S(\mathbf{r}), \end{aligned} \quad (2.5)$$

where $\boldsymbol{\kappa}(\mathbf{r}) = \boldsymbol{\delta} + \boldsymbol{\chi}(\mathbf{r})$ is the relative dielectric constant, and $\boldsymbol{\delta}$ is the Dirac delta function.

The physical variables in Eq. (2.5) describe vectors or tensors. Accordingly, we can rewrite the electric displacement in terms of components of vectors and tensors using Einstein notation:

$$D_i(\mathbf{r}, \mathbf{E}) = \varepsilon_0 \kappa_{ij}(\mathbf{r}) E_j(\mathbf{r}) + P_i^S(\mathbf{r}). \quad (2.6)$$

The electric displacement is written in terms of spontaneous polarization since it is this quantity which is commonly used in the Landau theory of ferroelectrics [14,23,24]. It is convenient to introduce the dielectric inhomogeneity through a position-dependent relative dielectric constant $\kappa_{ij}(\mathbf{r})$. The electrostatic equilibrium equation in the Maxwell equations indicates that the gradient of the electric displacement equals the position-dependent free charge density, i.e.

$$\frac{\partial D_i(\mathbf{r}, \mathbf{E})}{\partial x_i} = \frac{\partial [\varepsilon_0 \kappa_{ij}(\mathbf{r}) E_j(\mathbf{r}) + P_i^S(\mathbf{r})]}{\partial x_i} = \rho_f(\mathbf{r}). \quad (2.7)$$

To solve Eq. (2.7) we introduce another physical variable $\varphi(\mathbf{r})$, called the “depolarization potential”, related to the depolarization field by $E_j^d(\mathbf{r}) = -\frac{\partial \varphi(\mathbf{r})}{\partial x_j}$. Using this substitution and Eq. (2.4), Eq. (2.7) becomes

$$\frac{\partial \left[\varepsilon_0 \kappa_{ij}(\mathbf{r}) \left(E_j^{\text{ext}} - \frac{\partial \varphi(\mathbf{r})}{\partial x_j} \right) + P_i^S(\mathbf{r}) \right]}{\partial x_i} = \rho_f(\mathbf{r}). \quad (2.8)$$

We write the position-dependent relative dielectric constant as the sum of the homogeneous reference κ_{ij}^0 and inhomogeneous perturbation $\Delta\kappa_{ij}(\mathbf{r})$, i.e.

$$\kappa_{ij}(\mathbf{r}) = \kappa_{ij}^0 + \Delta\kappa_{ij}(\mathbf{r}), \quad (2.9)$$

Substituting Eq. (2.9) into Eq. (2.8) and rearranging we obtain

$$\begin{aligned} \kappa_{ij}^0 \frac{\partial^2 \varphi(\mathbf{r})}{\partial x_i \partial x_j} &= \frac{\partial}{\partial x_i} \left[\Delta\kappa_{ij}(\mathbf{r}) \left(E_j^{\text{ext}} - \frac{\partial \varphi(\mathbf{r})}{\partial x_j} \right) \right] \\ &+ \frac{1}{\varepsilon_0} \frac{\partial P_i^S(\mathbf{r})}{\partial x_i} - \frac{\rho_f(\mathbf{r})}{\varepsilon_0}. \end{aligned} \quad (2.10)$$

Eq. (2.10) is the key electrostatic equilibrium equation for an electrically inhomogeneous system. Assuming periodic boundary conditions Eq. (2.10) can be numerically solved using the fast Fourier transform and spectral iterative method for zero order, first order, or higher order approximations as outlined below.

2.1. Zero order approximation

Assuming the dielectric constants to be homogeneous so that $\Delta\kappa_{ij}(\mathbf{r})$ is 0 in Eq. (2.10) we have

$$\kappa_{ij}^0 \frac{\partial^2 \varphi^0(\mathbf{r})}{\partial x_i \partial x_j} = \frac{1}{\varepsilon_0} \frac{\partial P_i^S(\mathbf{r})}{\partial x_i} - \frac{\rho_f(\mathbf{r})}{\varepsilon_0}. \quad (2.11)$$

In Fourier space

$$-\kappa_{ij}^0 q_i q_j \tilde{\varphi}^0(\mathbf{q}) = \frac{I}{\varepsilon_0} q_i \tilde{P}_i^S(\mathbf{q}) - \frac{\tilde{\rho}_f(\mathbf{q})}{\varepsilon_0}, \quad (2.12)$$

where $\tilde{\varphi}^0(\mathbf{q})$, $\tilde{P}_i^S(\mathbf{q})$, and $\tilde{\rho}_f(\mathbf{q})$ are the Fourier transforms of $\varphi^0(\mathbf{r})$, $P_i^S(\mathbf{r})$, and $\rho_f(\mathbf{r})$, respectively, and q_j is the j th component of the reciprocal lattice vector. Solving Eq. (2.12) we get

$$\tilde{\varphi}^0(\mathbf{q}) = -\frac{I}{\varepsilon_0} G(\mathbf{q}) q_i \tilde{P}_i^S(\mathbf{q}) + G(\mathbf{q}) \frac{\tilde{\rho}_f(\mathbf{q})}{\varepsilon_0}, \quad (2.13)$$

where $G(\mathbf{q})^{-1} = \kappa_{ij}^0 q_i q_j$. Taking the inverse Fourier transform of both sides of Eq. (2.13) we obtain the zero order approximation of the depolarization potential,

$$\varphi^0(\mathbf{r}) = -\frac{1}{\varepsilon_0} \int \frac{d^3 q}{(2\pi)^3} G(\mathbf{q}) (I q_i \tilde{P}_i^S(\mathbf{q}) - \tilde{\rho}_f(\mathbf{q})) e^{i\mathbf{q}\cdot\mathbf{r}}. \quad (2.14)$$

The zero order depolarization field is then given by

$$E_j^{\text{d}-0}(\mathbf{r}) = -\int \frac{d^3 q}{(2\pi)^3} I q_j \tilde{\varphi}^0(\mathbf{q}) e^{i\mathbf{q}\cdot\mathbf{r}}. \quad (2.15)$$

2.2. First order approximation

Substituting the zero order depolarization potential (Eq. (2.14)) and depolarization field (Eq. (2.15)) into Eq. (2.10)

we obtain the first order solution for the depolarization potential

$$\begin{aligned} \kappa_{ij}^0 \frac{\partial^2 \varphi^1(\mathbf{r})}{\partial x_i \partial x_j} &= \frac{\partial}{\partial x_i} \left[\Delta\kappa_{ij}(\mathbf{r}) \left(E_j^{\text{ext}} + E_j^{\text{d}-0}(\mathbf{r}) \right) \right] \\ &+ \frac{1}{\varepsilon_0} \frac{\partial P_i^S(\mathbf{r})}{\partial x_i} - \frac{\rho_f(\mathbf{r})}{\varepsilon_0}. \end{aligned} \quad (2.16)$$

The solution of $\varphi^1(\mathbf{r})$ is obtained in Fourier space:

$$\begin{aligned} \tilde{\varphi}^1(\mathbf{q}) &= -IG(\mathbf{q}) q_i \{ \Delta\kappa_{ij}(\mathbf{r}) (E_j^{\text{ext}} + E_j^{\text{d}-0}(\mathbf{r})) \}_{\mathbf{q}} \\ &- \frac{I}{\varepsilon_0} G(\mathbf{q}) q_i \tilde{P}_i^S(\mathbf{q}) + G(\mathbf{q}) \frac{\tilde{\rho}_f(\mathbf{q})}{\varepsilon_0}, \end{aligned} \quad (2.17)$$

where $\{ \Delta\kappa_{ij}(\mathbf{r}) (E_j^{\text{ext}} + E_j^{\text{d}-0}(\mathbf{r})) \}_{\mathbf{q}}$ indicates the Fourier transforms of $\Delta\kappa_{ij}(\mathbf{r}) (E_j^{\text{ext}} + E_j^{\text{d}-0}(\mathbf{r}))$. The first order depolarization field in real space can be obtained from the potential by

$$E_j^{\text{d}-1}(\mathbf{r}) = -\int \frac{d^3 q}{(2\pi)^3} I q_j \tilde{\varphi}^1(\mathbf{q}) e^{i\mathbf{q}\cdot\mathbf{r}}. \quad (2.18)$$

2.3. Higher order approximation

Higher order solutions for $\varphi(\mathbf{r})$ are derived in a similar way as the first order approximation,

$$\begin{aligned} \kappa_{ij}^0 \frac{\partial^2 \varphi^n(\mathbf{r})}{\partial x_i \partial x_j} &= \frac{\partial}{\partial x_i} \left[\Delta\kappa_{ij}(\mathbf{r}) (E_j^{\text{ext}} + E_j^{\text{d}-(n-1)}(\mathbf{r})) \right] + \frac{1}{\varepsilon_0} \\ &\times \frac{\partial P_i^S(\mathbf{r})}{\partial x_i} - \frac{\rho_f(\mathbf{r})}{\varepsilon_0}. \end{aligned} \quad (2.19)$$

As with the solution for $\varphi^1(\mathbf{r})$, the solution for $\varphi^n(\mathbf{r})$ is solved using Fourier transforms:

$$\begin{aligned} \tilde{\varphi}^n(\mathbf{q}) &= -IG(\mathbf{q}) q_i \{ \Delta\kappa_{ij}(\mathbf{r}) (E_j^{\text{ext}} + E_j^{\text{d}-(n-1)}(\mathbf{r})) \}_{\mathbf{q}} \\ &- \frac{I}{\varepsilon_0} G(\mathbf{q}) q_i \tilde{P}_i^S(\mathbf{q}) + G(\mathbf{q}) \frac{\tilde{\rho}_f(\mathbf{q})}{\varepsilon_0}. \end{aligned} \quad (2.20)$$

Higher order approximations of the depolarization field can be obtained from

$$E_j^{\text{d}-n}(\mathbf{r}) = -\int \frac{d^3 q}{(2\pi)^3} I q_j \tilde{\varphi}^n(\mathbf{q}) e^{i\mathbf{q}\cdot\mathbf{r}}. \quad (2.21)$$

The total electric potential $\Phi(\mathbf{r})$ can be calculated from the electric fields via $E_j^{\text{ext}} + E_j^{\text{d}}(\mathbf{r}) = -\frac{\partial \Phi(\mathbf{r})}{\partial x_j}$. Using the inverse Fourier transforms we have

$$\Phi(\mathbf{r}) = \int \frac{d^3 q}{(2\pi)^3} I q_j^{-1} \{ E_j^{\text{ext}} + E_j^{\text{d}}(\mathbf{r}) \}_{\mathbf{q}} e^{i\mathbf{q}\cdot\mathbf{r}}. \quad (2.22)$$

It should be emphasized again that the above formulation for solving the electrostatic Poisson equation is applicable only under the assumption of the harmonic approximation and of an electric field-independent dielectric constant. For instance, this formalism can be used to solve the electrostatic equilibrium equation in linear dielectrics or dielectric composites. In the phase field model of ferroelectrics the soft mode contribution to the dielectric constant has already been included in the Landau free energy as a

function of polarization [25]. This soft mode contribution to the dielectric constant depends on the electric field. However, there is still a contribution from hard modes, which is non-zero far from the transition temperature and was called the background dielectric constant by Tagantsev [25]. This background dielectric constant is usually independent of the electric field. Only this background dielectric constant is explicitly included in the Poisson equation in the phase field model of ferroelectrics [24], and thus the proposed SPM described above can be used to solve the Poisson equation in the following phase field model of nanoferroelectrics.

3. Phase field model of ferroelectric nanoparticles

Periodic boundary conditions cannot be directly used for nanoparticles. Therefore, we employed an extended computational cell with the nanoparticles surrounded by a vacuum [5,26], as shown in Fig. 1. In the phase field model the temporal domain structure evolution is described by the time-dependent Landau–Ginzburg (TDGL) equation:

$$\frac{\partial \mathbf{P}(\mathbf{r}, t)}{\partial t} = -L \frac{\delta F}{\delta \mathbf{P}(\mathbf{r}, t)}, \quad (3.1)$$

where $\mathbf{P}(\mathbf{r}, t)$ is the spontaneous polarization field, L is a kinetic coefficient that is related to the domain wall mobility, and F is the total free energy of the system. The total free energy includes the bulk energy, elastic energy, electric energy, and gradient energy:

$$F = \iiint_V (f_{\text{bulk}} + f_{\text{elastic}} + f_{\text{electric}} + f_{\text{grad}}) dV. \quad (3.2)$$

The bulk free energy density for PbTiO_3 is described by a sixth order Landau–Devonshire polynomial:

$$\begin{aligned} f_{\text{bulk}} = & \alpha_1 (P_1^2 + P_2^2 + P_3^2) + \alpha_{11} (P_1^4 + P_2^4 + P_3^4) \\ & + \alpha_{12} (P_1^2 P_2^2 + P_1^2 P_3^2 + P_2^2 P_3^2) + \alpha_{112} [P_1^4 (P_2^2 + P_3^2) \\ & + P_2^4 (P_1^2 + P_3^2) + P_3^4 (P_1^2 + P_2^2)] + \alpha_{111} (P_1^6 + P_2^6 + P_3^6) \\ & + \alpha_{123} P_1^2 P_2^2 P_3^2, \end{aligned} \quad (3.3)$$

where all of the coefficients were fitted to bulk properties at zero stress and, except for α_1 , are independent of temperature.

The elastic energy density is given by:

$$\begin{aligned} f_{\text{elastic}} = & \frac{1}{2} c_{ijkl}(\mathbf{r}) e_{ij}(\mathbf{r}) e_{kl}(\mathbf{r}) \\ = & \frac{1}{2} c_{ijkl}(\mathbf{r}) (\varepsilon_{ij}(\mathbf{r}) - \varepsilon_{ij}^0(\mathbf{r})) (\varepsilon_{kl}(\mathbf{r}) - \varepsilon_{kl}^0(\mathbf{r})), \end{aligned} \quad (3.4)$$

where $c_{ijkl}(\mathbf{r})$ is the component of the position-dependent elastic stiffness tensor, $e_{ij}(\mathbf{r})$ is the elastic strain, $\varepsilon_{ij}(\mathbf{r})$ is the total strain, and $\varepsilon_{ij}^0(\mathbf{r})$ is the eigenstrain or transformation strain. Using the cubic phase as the reference the spontaneous strain $\varepsilon_{ij}^0(\mathbf{r})$ can be expressed by the electrostrictive coefficients and polarizations as $\varepsilon_{ij}^0(\mathbf{r}) = Q_{ijkl}(\mathbf{r}) P_k(\mathbf{r}) P_l(\mathbf{r})$. Here the Einstein summation convention for the repeated indices is employed and $i, j, k, l = 1, 2, 3$. According to Khachatryan's elastic theory the total strain $\varepsilon_{ij}(\mathbf{r})$ may be

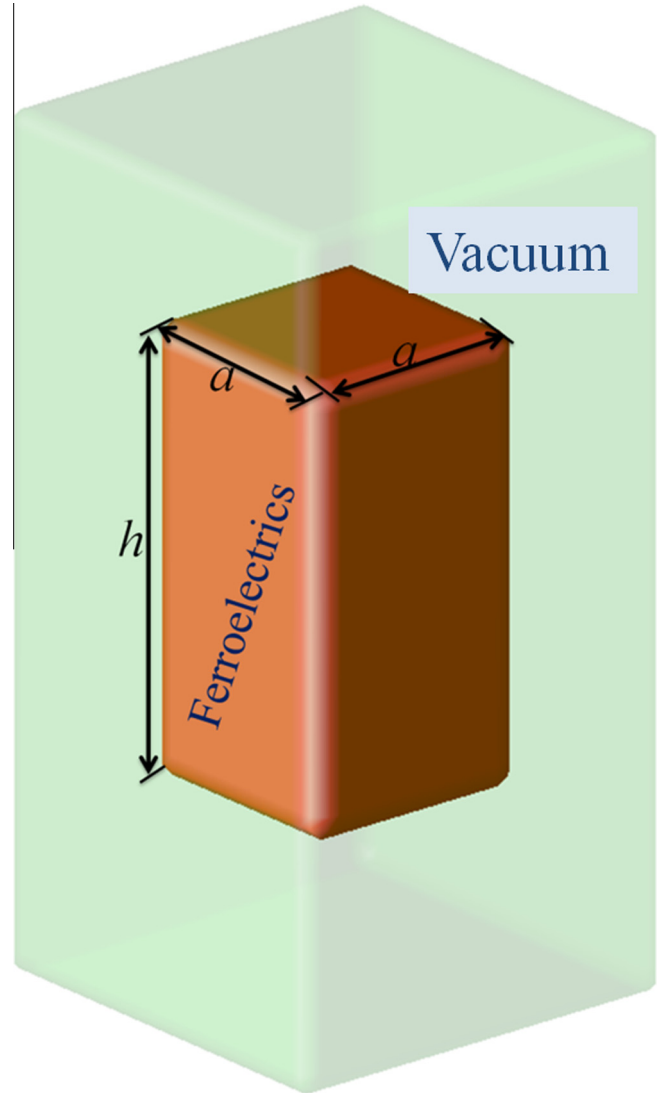


Fig. 1. Three-dimensional schematic illustration of the nanoparticles in the simulation with a , a , and h indicating the length, width, and thickness, respectively.

expressed as the sum of homogeneous and heterogeneous strains, i.e. $\varepsilon_{ij}(\mathbf{r}) = \bar{\varepsilon}_{ij} + \delta\varepsilon_{ij}(\mathbf{r})$ [27]. The homogeneous strain is defined in such a way that $\int \delta\varepsilon_{ij}(\mathbf{r}) dV = 0$, which represents the macroscopic shape change of a system generated due to the formation of a domain structure. The heterogeneous strain does not change the macroscopic shape of a system, and it can be calculated from $\delta\varepsilon_{ij}(\mathbf{r}) = (\partial u_i(\mathbf{r}) / \partial x_j + \partial u_j(\mathbf{r}) / \partial x_i) / 2$, where $u_i(\mathbf{r})$ are the components of the position-dependent displacement. We solved the mechanical equilibrium equation $\sigma_{ij,j} = 0$ for an elastic inhomogeneity system using the SPM to obtain the equilibrium elastic field [19], as shown in Appendix A.

Homogeneous strain in the system was determined by the mechanical boundary conditions. For constant strain boundary conditions the homogeneous strain $\bar{\varepsilon}_{ij}$ was taken to equal the externally applied strain $\varepsilon_{ij}^{\text{app}}$. For constant stress boundary conditions the homogeneous strain was determined from [28]:

$$\bar{\varepsilon}_{ij} = \langle s_{ijkl}(\mathbf{r}) \rangle (\sigma_{kl}^{\text{app}} + \langle c_{klmn}(\mathbf{r}) \varepsilon_{mn}^0(\mathbf{r}) \rangle - \langle c_{klmn}(\mathbf{r}) \delta \varepsilon_{mn}(\mathbf{r}) \rangle), \quad (3.5)$$

where $\langle \rangle$ represents the volume average of the component.

Due to the high surface to volume ratio for nanoparticles contributions from surface stress can be significant in determining the phase transitions and domain structures. The surface stress is dependent on the particle shape. For instance, the surface stress for a spherical particle is $\sigma_{ij} = -p(i=j)$ and $\sigma_{ij} = 0(i \neq j)$, whereas for cylindrical particles such as nanorods and nanowires it is $\sigma_{11} = \sigma_{22} = -p_1$, $\sigma_{33} = -p_3$, $\sigma_{ij} = 0(i \neq j)$. Here p is the compressive stress of a spherical particle, p_1 is the biaxial compressive stress along the 11 and 22 direction of cylindrical particles, and p_3 is the compressive stress along the 33 direction of the cylindrical particles. The surface tension plays a role similar to hydrostatic pressure for a sphere, and to biaxially compressive stress for a cylinder. It was concluded in previous experimental and theoretical works that the surface stress is proportional to the curvature of the surface, such that $p = \frac{\mu}{r}$ [13,29,30], where μ is determined by the two media on either side of the interface and typically has a value between 1 and 50 N m⁻¹ [13,31]. In this work we use a cuboidal shape model for simplicity and relate the surface stress to the size by [31]:

$$\sigma_{11} = \sigma_{22} = -\frac{\mu_1}{a}, \sigma_{33} = -\frac{\mu_2}{h}, \sigma_{12} = \sigma_{13} = \sigma_{23} = 0, \quad (3.6)$$

where μ_1 is the surface stress coefficient of the lateral surface, μ_2 is the surface stress coefficients of the bottom/top surfaces, a is the length and width of the nanoparticles, and h is the height of the nanoparticles. This surface tension is equivalent to an externally applied compressive stress on the nanoparticles of

$$\sigma_{11}^{\text{app}} = \sigma_{22}^{\text{app}} = -\frac{\mu_1}{a}, \sigma_{33}^{\text{app}} = -\frac{\mu_2}{h}, \sigma_{12}^{\text{app}} = \sigma_{13}^{\text{app}} = \sigma_{23}^{\text{app}} = 0. \quad (3.7)$$

The induced homogeneous strain can be calculated by substituting Eq. (3.7) into Eq. (3.5). With the solution to the mechanical equilibrium equation the elastic energy density can be calculated using the expression

$$f_{\text{elastic}} = \frac{1}{2} c_{ijkl}(\mathbf{r}) (\bar{\varepsilon}_{ij} + \delta \varepsilon_{ij}(\mathbf{r}) - Q_{ijmn}(\mathbf{r}) P_m(\mathbf{r}) P_n(\mathbf{r})) \times (\bar{\varepsilon}_{kl} + \delta \varepsilon_{kl}(\mathbf{r}) - Q_{klmn}(\mathbf{r}) P_m(\mathbf{r}) P_n(\mathbf{r})). \quad (3.8)$$

The electrostatic energy density of a given domain structure is calculated using [23,25,32–34]

$$f_{\text{electric}} = -\mathbf{P}(\mathbf{r}) \cdot \mathbf{E} - \frac{1}{2} \varepsilon_0 \kappa^{\text{b}}(\mathbf{r}) \mathbf{E}^2 = -P_i(\mathbf{r}) E_i(\mathbf{r}) - \frac{1}{2} \varepsilon_0 \kappa_{ij}^{\text{b}}(\mathbf{r}) E_i(\mathbf{r}) E_j(\mathbf{r}), \quad (3.9)$$

where $\kappa_{ij}^{\text{b}}(\mathbf{r})$ is the position-dependent background dielectric constant tensor. Assuming no space charge inside the nanoparticles, the electric displacement

$$D_i(\mathbf{r}) = \varepsilon_0 \kappa_{ij}^{\text{b}}(\mathbf{r}) E_j(\mathbf{r}) + P_i(\mathbf{r}) \quad (3.10)$$

satisfies the electrostatic equilibrium equation

$$\partial D_i(\mathbf{r}) / \partial x_i = 0, \quad (3.11)$$

which can be solved by the proposed SPM. In previous phase field models on ferroelectrics, the dielectric inhomogeneity was described using an inhomogeneous distribution of the Landau–Devonshire polynomial coefficients [24,35,36] and a homogeneous background dielectric constant was assumed in the electrostatic equilibrium equation. The effect of an inhomogeneous background dielectric constant will be discussed in Section 4.1 by comparing the electric field solutions.

The gradient energy density in an anisotropic system can be expressed as:

$$f_{\text{grad}} = \frac{1}{2} \gamma_{ijkl} P_{i,j} P_{k,l}, \quad (3.12)$$

where γ_{ijkl} is the gradient energy coefficient and $P_{i,j} = \partial P_i / \partial x_j$. For an isotropic system Eq. (3.12) can be rewritten as

$$f_{\text{grad}} = \frac{1}{2} \gamma_{11} (P_{1,1}^2 + P_{2,2}^2 + P_{3,3}^2 + P_{1,2}^2 + P_{2,1}^2 + P_{1,3}^2 + P_{3,1}^2 + P_{2,3}^2 + P_{3,2}^2), \quad (3.13)$$

where γ_{ij} is related to γ_{ijkl} by the Vogit's notion and $\gamma_{12} = 0$, $\gamma_{11} = 2\gamma_{44}$ in an isotropic system.

With the total free energy density Eq. (3.1) can be solved in Fourier space with a given polarization boundary condition. The generalized boundary condition for polarization due to the surface or size effect can be written as a linear combination of the polarization and its gradient at the surface, i.e. $(C_1 d\mathbf{P}/d\mathbf{n} + C_2 \mathbf{P})|_{\text{on the surface}} = 0$, where C_1 and C_2 are constants determined by the degree of charge compensation on the surface. If there is full compensation of charges on the surface the polarization is homogeneous across the surface, leading to $C_2 = 0$, $C_1 \neq 0$, and if there is no compensation of charges on the surface polarization should be) at the surface, leading to $C_1 = 0$, $C_2 \neq 0$. In most cases the interface is partially compensated, leading to the polarization boundary conditions [13,37,38]

$$\left(\frac{d\mathbf{P}}{d\mathbf{n}} + \frac{\mathbf{P}}{\delta} \right)_{\text{on the surface}} = 0, \quad (3.14)$$

where \mathbf{n} is the interface normal unit vector and δ is the so-called extrapolation length describing the polarization difference between the interface and bulk. Using the second order finite difference approximation to find the derivative ($d\mathbf{P}/d\mathbf{n}$), Eq. (3.14) may be discretized as [39,40]:

$$\begin{aligned} \mathbf{P}(x_1, y, z) &= \frac{4\mathbf{P}(x_1 + \Delta x, y, z) - \mathbf{P}(x_1 + 2\Delta x, y, z)}{3 + \lambda_x}, \\ \mathbf{P}(x_2, y, z) &= \frac{4\mathbf{P}(x_2 - \Delta x, y, z) - \mathbf{P}(x_2 - 2\Delta x, y, z)}{3 + \lambda_x}, \\ \mathbf{P}(x, y_1, z) &= \frac{4\mathbf{P}(x, y_1 + \Delta y, z) - \mathbf{P}(x, y_1 + 2\Delta y, z)}{3 + \lambda_y}, \\ \mathbf{P}(x, y_2, z) &= \frac{4\mathbf{P}(x, y_2 - \Delta y, z) - \mathbf{P}(x, y_2 - 2\Delta y, z)}{3 + \lambda_y}, \\ \mathbf{P}(x, y, z_1) &= \frac{4\mathbf{P}(x, y, z_1 + \Delta z) - \mathbf{P}(x, y, z_1 + 2\Delta z)}{3 + \lambda_z}, \\ \mathbf{P}(x, y, z_2) &= \frac{4\mathbf{P}(x, y, z_2 - \Delta z) - \mathbf{P}(x, y, z_2 - 2\Delta z)}{3 + \lambda_z}, \end{aligned} \quad (3.15)$$

where $\lambda_x = 2\Delta x/\delta_x$, $\lambda_y = 2\Delta y/\delta_y$, $\lambda_z = 2\Delta z/\delta_z$, $x = x_1$ and $x = x_2$ represent the two interfaces perpendicular to the [100] direction, $y = y_1$ and $y = y_2$ represent the two interfaces perpendicular to the [010] direction, and $z = z_1$ and $z = z_2$ represent the two interfaces perpendicular to the [001] direction of a nanoparticle.

4. Results and discussion

In order to test the accuracy of the proposed SPM we first employed two electrostatically inhomogeneous systems as examples: (1) an infinite ferroelectric plate with spontaneous polarization \mathbf{P}^S surrounded by a vacuum; (2) a ferroelectric sphere with spontaneous polarization \mathbf{P}^S surrounded by a vacuum. In these examples the soft and hard mode contributions to the dielectric constant were not divided since we did not evolve the polarization. We solved Eq. (2.10) directly to obtain the electric field with the full dielectric constant as input. We then compared the numerical results with analytical results for these cases.

Finally, we employed the method to calculate the effects of size and shape on the phase transitions and domain structures of PbTiO_3 ferroelectric nanoparticles. In this case a position-dependent background dielectric constant was used because the polarization was evolved in the phase field model of ferroelectric nanoparticles.

4.1. Infinite dielectric plate in a vacuum

We considered a ferroelectric plate with parallel surfaces perpendicular to the x -direction extending infinitely in the y - and z -directions, as shown in Fig. 2a. This plate was free-standing in a vacuum without an external electric field (i.e. $\mathbf{E}_{\text{ext}} = 0$). We assumed this ferroelectric plate had a spontaneous polarization of $P^S = 100 \mu\text{C m}^{-2}$ along the x -direction. Due to the infinite extension along y - and z -directions this problem can be regarded as quasi one-dimensional. We used a large enough number of grid points N_x in the simulation to alleviate any image effect from the periodic boundary conditions. We used an isotropic relative dielectric constant tensor with a value of 100 for the ferroelectric plate. The SPM results were compared with the analytical solutions (ANA) to validate the accuracy of the scheme.

The solutions for the electric potential, field, and displacement along the A–A cross-section of the plate are shown in Fig. 2b–d. It can be seen that the electric displacement is 0 everywhere because there is no free charge. The electric displacement across the interface with the air and ferroelectric plates should be continuous. As shown in Fig. 2c, the electric field should be 0 in the vacuum according to $\mathbf{D} = \epsilon_0 \mathbf{kE} + \mathbf{P}^S$, as \mathbf{D} and \mathbf{P}^S are 0 in the vacuum. The numerical simulation using the present iterative perturbation scheme shows that the electric field in the plate has a homogeneous value of $-1.1294 \times 10^5 \text{ V m}^{-1}$, which agrees with the analytical solution that $E_{\text{inside}} = P^S/\epsilon_0$.

$\kappa = -1.1294 \times 10^5 \text{ V m}^{-1}$. In this example we did not consider an external electric field, so the calculated electric field is the depolarization field which has an opposite direction to the spontaneous polarization.

4.2. An isolated ferroelectric sphere in a vacuum

In order to study an isolated ferroelectric sphere in a vacuum, as shown in Fig. 3a, we assumed that the radius of the ferroelectric sphere was much smaller than the simulation box size to minimize the effect of periodic images on the solutions. In this work we assigned a radius (R_0) of the ferroelectric sphere of 16 grid points and a simulation size of $128 \times 128 \times 128$ grid points to give the ratio $R_0/N_x = 0.125$. We assumed the ferroelectric sphere to have a spontaneous polarization $P^S = 100 \mu\text{C m}^{-2}$ along the x -direction and an isotropic relative dielectric constant tensor of 100.

To reduce the Gibbs effect related to the Fourier transforms of functions across the sharp interface between the ferroelectric and vacuum we introduced a diffuse interface shaped function to describe the interfacial region between the vacuum and the ferroelectric in the form:

$$\eta(\mathbf{r}) = \frac{1}{2} \{1.0 - \tanh[\beta(d(\mathbf{r}) - R_0)]\}, \quad (4.1)$$

where $d(\mathbf{r})$ is the distance of any point (x, y) from the center of the sphere, and β is a positive parameter controlling the width of the surface.

The analytical solution for the electrostatic equilibrium equation in this example can be obtained from the Poisson equation with the boundary conditions:

$$\varphi(\mathbf{r}) = \begin{cases} \frac{P^S}{3\epsilon_0} x, & r \leq R_0 \\ \frac{R_0^2 P^S}{3\epsilon_0} \cdot \frac{x}{r^3}, & r \geq R_0 \end{cases} \quad (4.2)$$

where $r = \sqrt{x^2 + y^2 + z^2}$. It can be seen from Fig. 3b and c that, except for slight discrepancies at the simulation boundary and ferroelectric boundary, the numerical solutions of the electric potential and field agree well with the analytical results through both the A–A and B–B cross-sections. In both cases inside the ferroelectric ball the electric field is homogeneous and, in the absence of an external electric field equals the depolarization field induced by interruption of the spontaneous polarization at the surface of the sphere. The electric field has a maximal values at the surfaces along the A–A cross-section and decreases to 0 in a vacuum far from the ferroelectric. Differences between the numerical and the analytical solutions around the boundary stem from the fact that the numerical solutions were obtained with periodic boundary conditions with a diffuse interface description for the surface, while the analytical solution was for an isolated sphere in an infinite matrix with a sharp interface description.

Since each order of approximation for the electric solution was obtained analytically (see Eqs. (2.15) and (2.18)) the proposed algorithm was extremely efficient. Fig. 3d

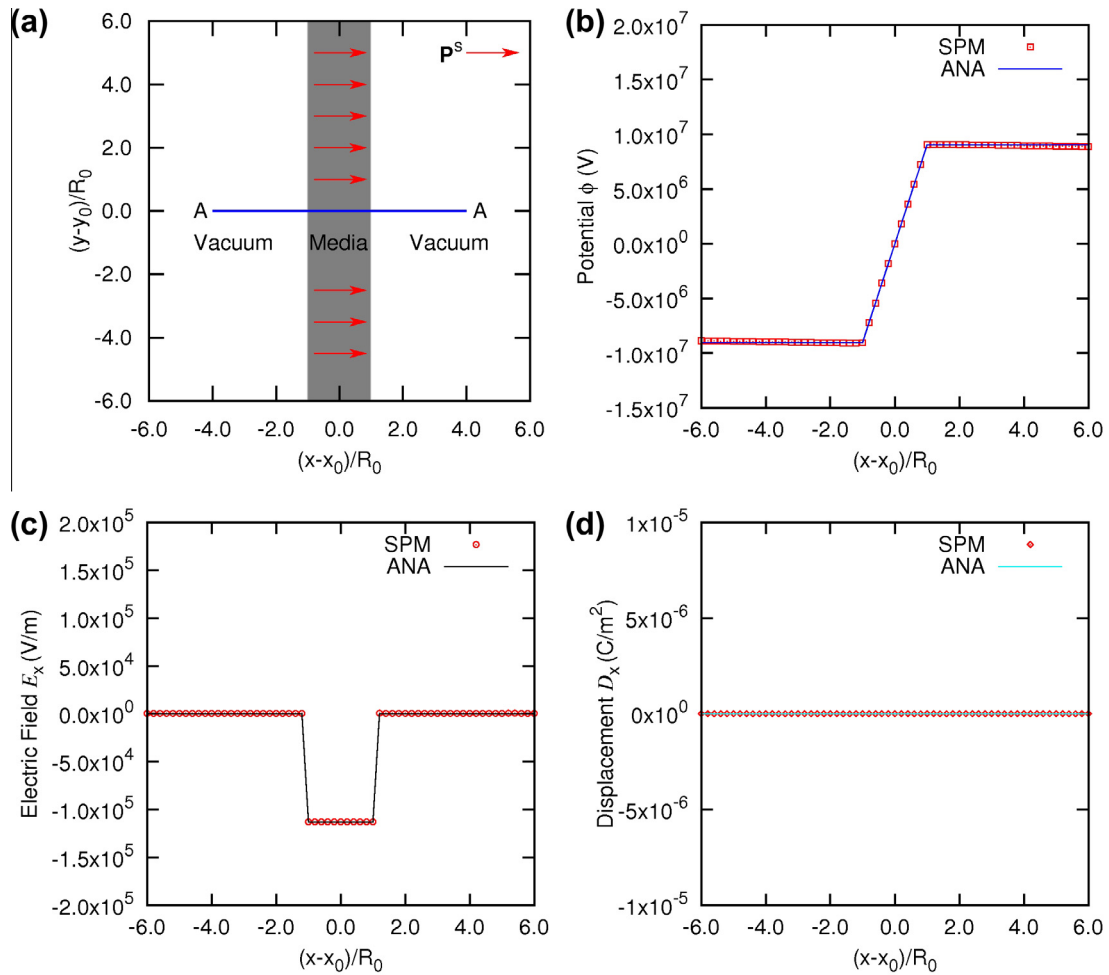


Fig. 2. (a) Schematics of an infinite ferroelectric plate with self-polarization \mathbf{P}^S in a vacuum, where R_0 indicates the half-width of the plate. (b) Electric potential ϕ along the A–A cross-section calculated by the SPM compared with the analytical solution. (c) Electric field component E_x along the A–A cross-section calculated by the SPM compared with the analytical solution. (d) Electric displacement component D_x along the A–A cross-section calculated by the SPM compared with the analytical solution.

shows the electric potential solution along the A–A cross-section at several iteration steps in the solution. It can be seen that the solutions higher than zero order are very close to each other. Thus a first order solution is a very good approximation for this special case.

Next we extended the simulation of the ferroelectric nanosphere to include inhomogeneity in the polarization distribution using the method described above to examine the effect of the polarization response on the solution. As shown in Fig. 4, the electric field solutions along the A–A cross-section in Fig. 3a are compared by considering and not considering the dielectric inhomogeneity. One can see from Fig. 4 that the electric field solution obtained by considering only polarization inhomogeneity does not agree with the analytical result, whereas the result obtained by considering both the polarization inhomogeneity and dielectric constant inhomogeneity agrees with the analytical result to a large extent. In other words, for the present nanoparticle model with a vacuum covering the surface of the ferroelectric particles both the polarization inhomogeneity

and dielectric constant inhomogeneity have to be taken into account in order to obtain accurate electric solutions.

4.3. Phase transitions and domain structures of PbTiO_3 nanoparticles

We studied the effect of the aspect ratio (h/a) on the phase transitions, domain structures, and domain switching for PbTiO_3 nanoparticles with constant volume. The material constants for the Landau free energy and electrostrictive coefficients of PbTiO_3 are taken from the literature [41–45], i.e. $\alpha_1 = 3.8 \times 10^5 (T - 752) \text{ C}^{-2} \text{ m}^2 \text{ N}$, $\alpha_{11} = -7.3 \times 10^7 \text{ C}^{-4} \text{ m}^6 \text{ N}$, $\alpha_{12} = 7.5 \times 10^8 \text{ C}^{-4} \text{ m}^6 \text{ N}$, $\alpha_{111} = 2.6 \times 10^8 \text{ C}^{-6} \text{ m}^{10} \text{ N}$, $\alpha_{112} = 6.1 \times 10^8 \text{ C}^{-6} \text{ m}^{10} \text{ N}$, $\alpha_{123} = -3.7 \times 10^9 \text{ C}^{-6} \text{ m}^{10} \text{ N}$, $Q_{11} = 0.089 \text{ C}^{-2} \text{ m}^4$, $Q_{12} = -0.026 \text{ C}^{-2} \text{ m}^4$, $Q_{44} = 0.0675 \text{ C}^{-2} \text{ m}^4$. The elastic constants are $c_{11} = 1.796 \times 10^{11}$, $c_{12} = 7.937 \times 10^{10}$, $c_{44} = 1.111 \times 10^{11} (\text{Nm}^{-2})$ [46]. We assigned a value of 10 to the relative background dielectric constant of PbTiO_3 . The size of the nanoparticles

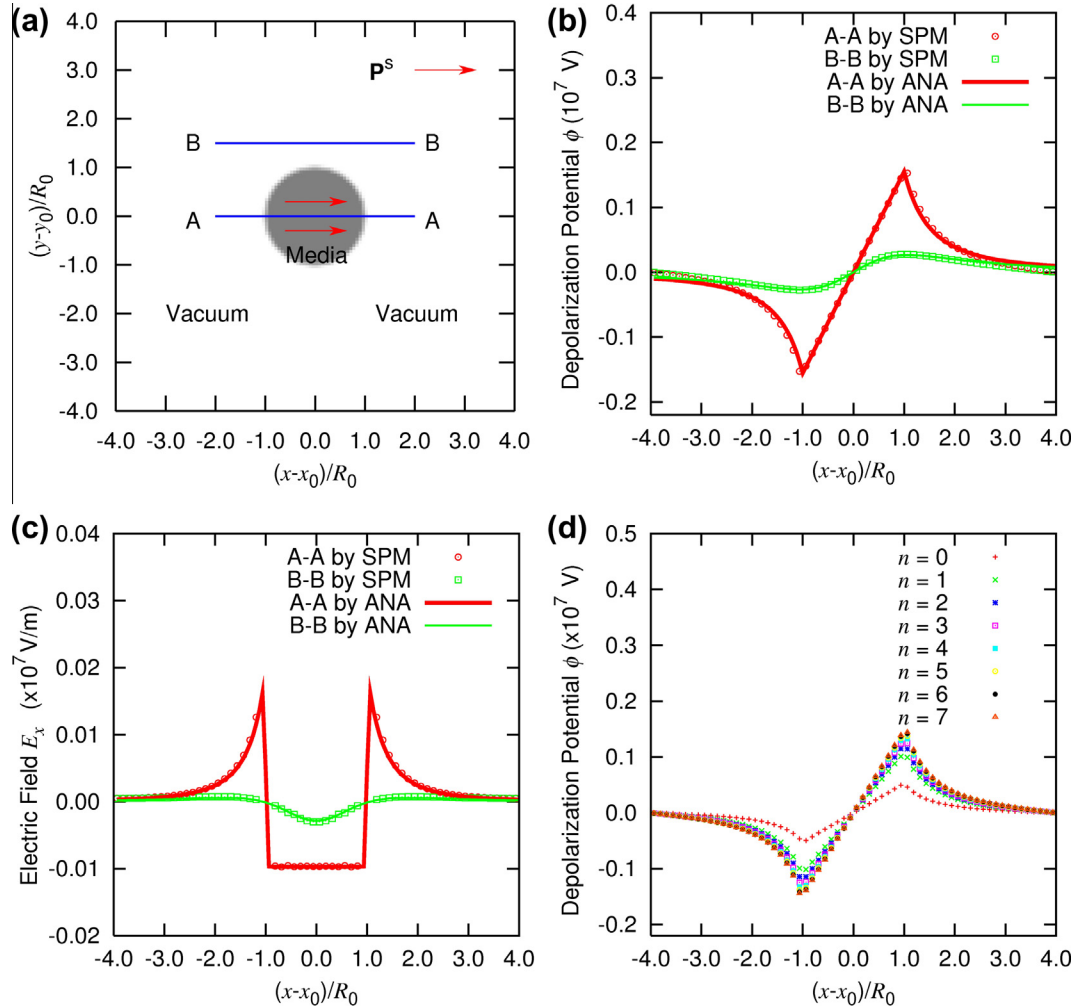


Fig. 3. (a). Schematics of the middle section (parallel to the x - y plane) of an isolated ferroelectric sphere with self-polarization \mathbf{P}^S along the x -direction surrounded by a vacuum, where R_0 indicates the radius of the sphere. (b) Electric potential ϕ along A–A and B–B cross-sections calculated from SPM compared with the analytic solution. (c) Electric field component E_x along the A–A and B–B cross-sections calculated by the SPM compared with the analytic solution. (d) Improved precision of the electric potential ϕ along the A–A cross-section was obtained through iteration of the SPM.

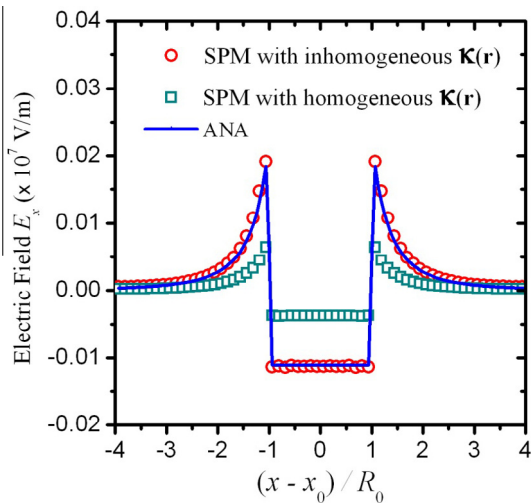


Fig. 4. Electric field solutions along the A–A cross-section in Fig. 3a obtained by considering and not considering the dielectric constant inhomogeneity, respectively, compared with the analytical result.

was $a = \Delta x \cdot N_x = \Delta y \cdot N_y$, and $h = \Delta z \cdot N_z$, where Δx , Δy , and Δz are the computational grid size, and $(N_x + 4) \times (N_y + 4) \times (N_z + 4)$ is the number of discrete grid points with the outer four layers of grids being the vacuum layer. The different shape of the nanoparticles can be achieved by changing the cell lengths (Δx , Δy , and Δz) or grid number (N_x , N_y , and N_z). The normalized isotropic gradient energy coefficient was assumed to have a value of 0.6. The extrapolation lengths (δ_x , δ_y , and δ_z), which describe the polarization difference between the interface and bulk, can be regarded as the respective thicknesses of the interfaces from a particular sense. In this work we assigned $\delta_x = \delta_y = \delta_z = 3$ nm, which was fitted from experimental measurement [38]. Surface stress coefficients of the lateral interface μ_1 and the top and bottom interfaces μ_2 were assumed to both be 4 N m^{-1} [31].

It should be noted that the electric and mechanical boundary conditions have significant effects on the equilibrium domain structures. As shown in Fig. 5, the difference

in elastic constants between a ferroelectric particle and the surrounding matrix (Fig. 5a) can strongly affect the stress distribution (Fig. 5b–d) within the particle [19], leading to an inhomogeneous polarization distribution due to the electrostrictive effect. In order to solve the electrostatic equilibrium equation (Eq. (2.9)) the boundary condition of the depolarization potential φ should be specified. In this simulation open-circuit boundary conditions were applied on each surface of the cuboidal particle, as shown in Fig. 1. The interfaces were automatically specified by treating the space outside the specimens as a vacuum to construct a periodic model so the proposed SPM can be used to solve the electrostatic equilibrium equation with a periodic depolarization potential on each boundary. When an external electric field E_3^{app} was applied along the x_3 -direction to study domain switching the total electro-

static potential was the sum of the periodic depolarization potential and the non-periodically applied potential, $-z \cdot E_3^{\text{app}}$. Similarly, the spectral iterative perturbation method with periodic displacements on each surface of the cuboid model was used to solve the mechanical equilibrium equation [19], as shown in Appendix A.

The complete temperature–shape phase diagram of PbTiO_3 nanoparticles with a constant volume of 32^3 nm^3 was constructed by numerically evolving the domain structures to equilibrium or near equilibrium as a function of h/a and temperature, as shown in Fig. 6. It can be seen from Fig. 6 that the Curie temperature of PbTiO_3 nanoparticle is enhanced in the rod ($4 \leq h/a \leq 16$) and wire ($h/a > 16$) shapes. This result agrees with the observations of Yadlovker and Berger for Roshelle salt nanorods ($h/a \approx 500 \text{ nm}/30 \text{ nm} \approx 16.67$) [47]. This enhancement of the Curie

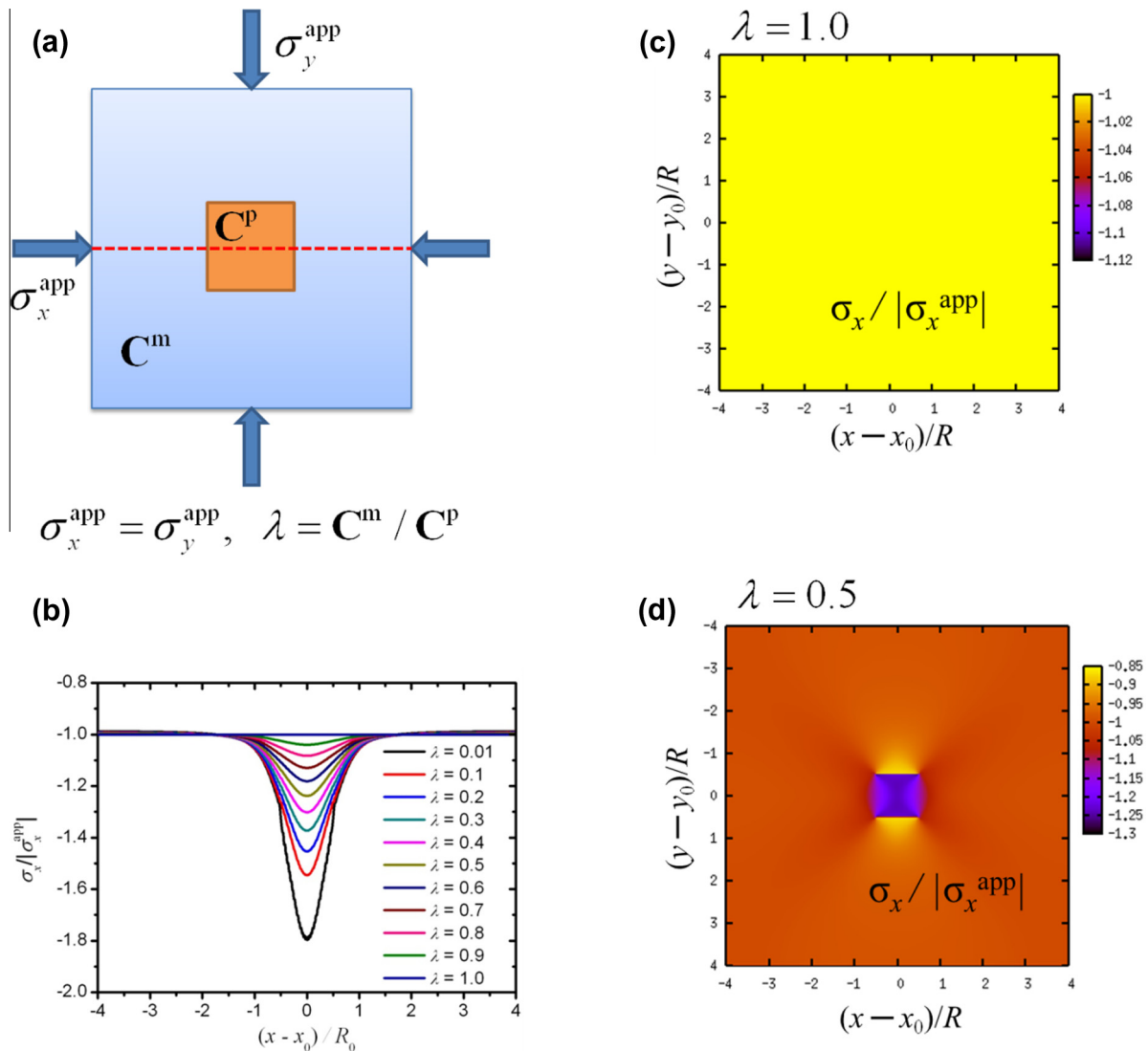


Fig. 5. (a). Schematics of the middle section (parallel to the x - y plane) of the present nanoparticle model, where C^p indicates the elastic constant tensor of the ferroelectric, C^m indicates the elastic constant tensor of the matrix, λ is the elastic inhomogeneity strength defined by $\lambda = C^m/C^p$, and σ_x^{app} and σ_y^{app} are the external stresses applied to the composite to study to elastic inhomogeneity strength effect on the stress distribution. (b) Different elastic inhomogeneity strengths resulted in different elastic stress solutions σ_x along the cross-section described by the red dash line in (a). (c) Homogeneous stress distribution obtained from the elastic inhomogeneity strength $\lambda = 1.0$. (d) Inhomogeneous stress distribution obtained from the elastic inhomogeneity strength $\lambda = 0.5$. (For interpretation of the references to colour in this figure legend, the reader is referred to the web version of this article.)

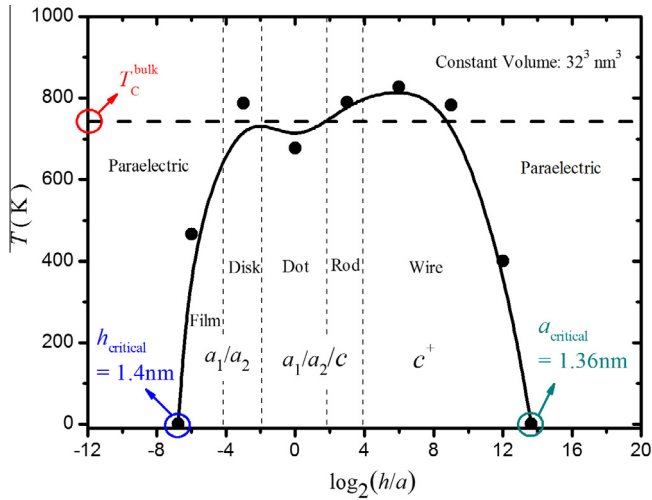


Fig. 6. Temperature–shape phase diagram of free-standing PbTiO_3 nanoparticles with a constant volume of 32^3 nm^3 , where h_{critical} and a_{critical} indicate the critical values for the thickness h and lateral length a of the nanoparticle model, respectively, and a_1 , a_2 , and c represent the domain orientations.

temperature was attributed to the large lateral pressure imposed by the surface stress, similar to the enhancement of the Curie temperature in equally biaxially compressed thin films [48,49]. At constant volume, with h/a continuously increasing from 64, the ferroelectric transition temperature begins to decrease. The ferroelectricity completely disappears when a decreases to a critical size of 1.36 nm, compared with 1.32 nm from extrapolation of the first principle results [50]. On the other hand, with the shape changing to an ultrathin film (small h/a) the same phenomenon takes place and h has a critical size of 1.4 nm, compared with 1.0 nm from extrapolation of the experimental results on epitaxial PbTiO_3 thin film [51]. For a nanodot with a size of $32 \times 32 \times 32 \text{ nm}$, the Curie temperature is lower than its bulk counterpart. This reduction in Curie temperature has been observed in experiments when the size of the nanosphere is smaller than 40 nm [52–54]. This reduction in Curie temperature for the nanodot originates from the surface tension, which creates the same effect as hydrostatic pressure [55].

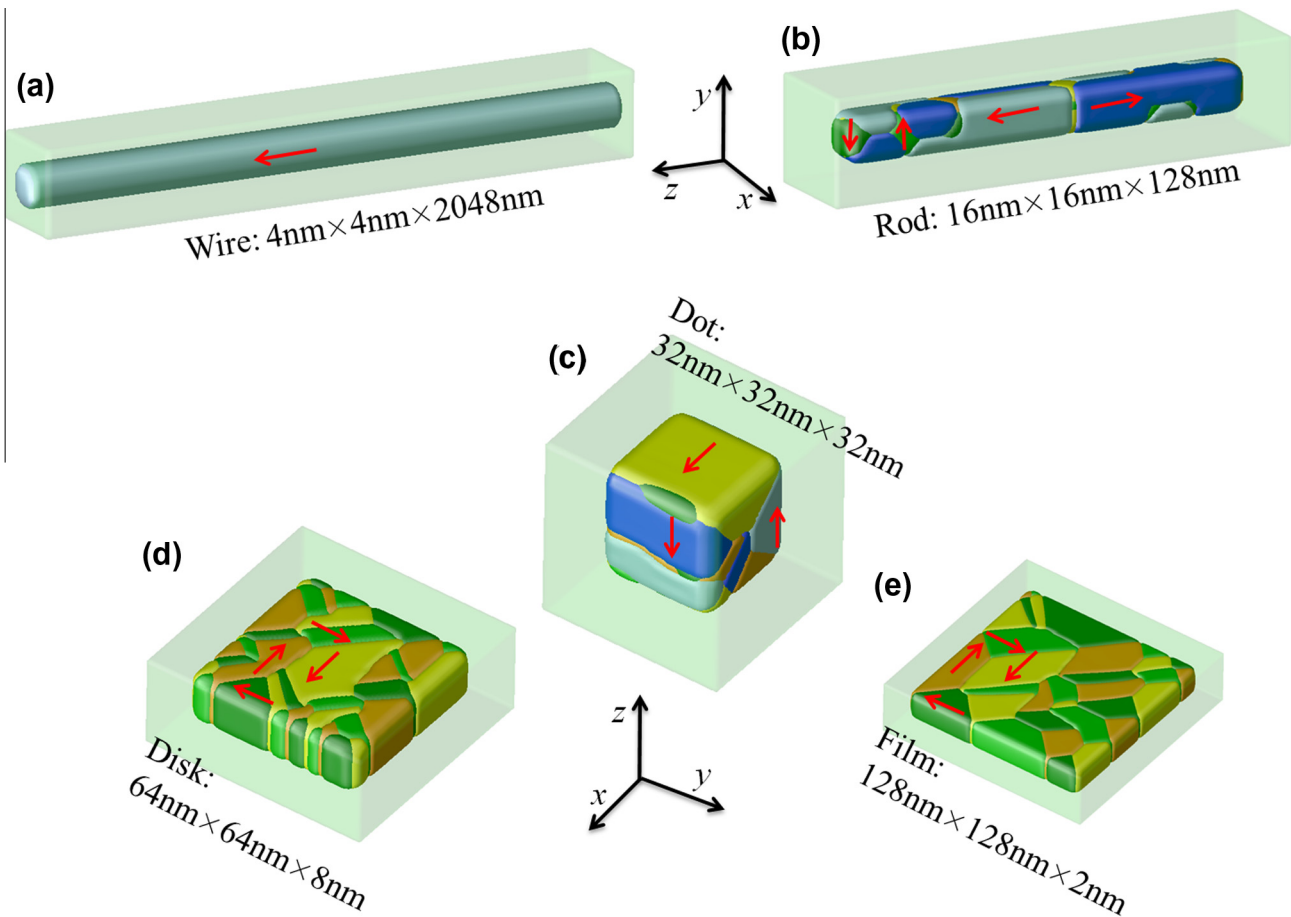


Fig. 7. Domain structures of PbTiO_3 nanoparticles with different shapes: (a) $4 \times 4 \times 2084 \text{ nm}$ nanowire; (b) with size $16 \times 16 \times 128 \text{ nm}$ nanorod; (c) $32 \times 32 \times 32 \text{ nm}$ nanodot; (d) $16 \times 16 \times 128 \text{ nm}$ nanodisk; (e) $128 \times 128 \times 2 \text{ nm}$ nanofilm. Yellow, orange, light green, dark green, light blue and darkblue indicate domain structures with polarization along the $[100]$, $[\bar{1}00]$, $[010]$, $[0\bar{1}0]$, $[001]$ and $[00\bar{1}]$ directions, respectively. (For interpretation of the references to color in this figure legend, the reader is referred to the web version of this article.)

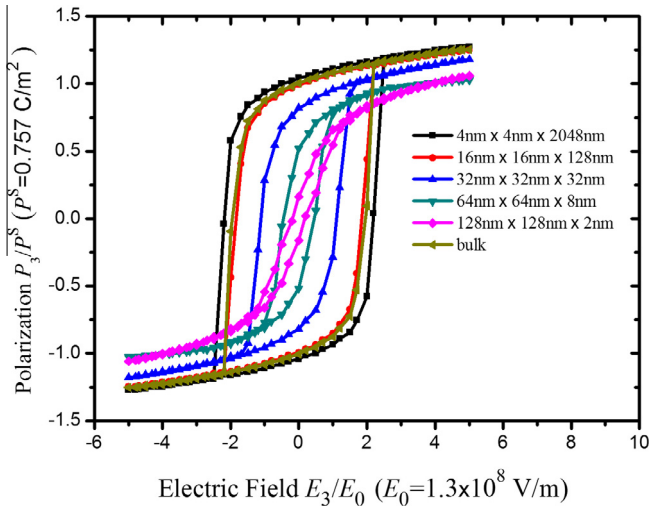


Fig. 8. Domain switching of PbTiO₃ nanoparticles with different shapes: (a) 4 × 4 × 2084 nm nanowire; (b) 16 × 16 × 128 nm nanorod; (c) 32 × 32 × 32 nm nanodot; (d) 16 × 16 × 128 nm nanodisk; (e) 128 × 128 × 2 nm nanofilm.

For nanoparticles from nanowires to ultrathin films the domain structures are expected to be dependent on the particle size, shape, and electrical boundary conditions, as shown in Fig. 7a–e. It can be seen from Fig. 7a that for a nanowire with a size of 4 × 4 × 2048 nm only a single c^+ (where the polarizations are along the axial direction of the wire) domain is stable, while for a nanorod with a size of 16 × 16 × 128 nm the domain structure includes many c domains and a few a_1/a_2 domains. In a nanowire with an axial dimension much longer than the lateral length the effect of lateral stress arising from the shape and size plays a more important role than the electric boundary condition in determining the domain structures, thus the extremely slender wire favors a single c^+ or c^- domain, as shown in Fig. 7a.

The diameter effect on the domain structure of a nanowire with a 2048 nm axial length was also investigated. It was found that with increasing diameter the domain structure transitions from a single c^+ or c^- domain to several c^+ and c^- domains at 18 nm. For a nanorod with a size equal to 16 × 16 × 28 nm the combined shape and electric boundary condition effects determine the domain structures. In the nanorod there are many c domains (volume fraction 0.84), which are favored by the lateral stress due to the rod shape, with a few a_1/a_2 domains (volume fraction 0.16) forming vortex domains favored by the open-circuit electric boundary conditions, as shown in Fig. 7b. Such vortex domain structures in ferroelectric nanorods under open-circuit electric boundary conditions have been found by first principles [5], in agreement with our work and other phase field simulation results [56,57]. In a nanodot with a size equal to 32 × 32 × 32 nm the surface tension plays the same role as hydrostatic pressure, rather than biaxial or uniaxial stress. Thus a_1/a_2 and c domains should coexist with similar volume fractions, and the simulation shows that the volume fractions of a_1/a_2 domains

and c domains are the same (both equal to 0.5), as shown in Fig. 7c. Similarly to the nanorods, domains assemble into vortex domain structures in the nanodot, which has also been observed experimentally [58] and verified by first principle calculations [59]. With further decreases in the aspect ratio c domains disappear and a_1/a_2 twin domains and some in-plane vortex domains become stable, as shown in Fig. 7d and e.

Fig. 8 shows the shape effect on domain switching in the PbTiO₃ nanoparticle. It can be seen that the coercive field, saturated polarization, and remnant polarization increase with aspect ratio under an externally applied electric field along the x_3 -direction. This effect can be attributed to an increased volume fraction of c domains inside the particle. A larger electric torque is needed from the externally applied electric field for 180° switching. In the nanodisk or thin film under open-circuit boundary conditions the uniaxially out-of-plane compressive stress originating from the surface tension makes the polarization lie along the in-plane directions. Thus under an externally applied electric field the polarization cannot be completely switched to out-of-plane, causing the saturated and remnant polarization to decrease.

5. Summary

A Fourier iterative SPM was proposed to solve the Poisson equation with inhomogeneous dielectric constant, polarization, and charge distributions. The proposed algorithm shows good accuracy on comparing numerical solutions for an infinite ferroelectric plate and an isolated ferroelectric sphere with analytical solutions. The proposed method was implemented in the phase field method to simulate shape and size effects on the phase transitions, domain structures, and domain switching in ferroelectric nanoparticles. The calculated temperature–shape phase diagrams of the nanoparticles show that the Curie temperature is increased in wire and rod shapes, but decreased in a dot shape. The simulated critical diameter and thickness for the nanowire and thin film are around 1.4 nm. Vortex domain structures are found to be stable in the nanorod, nanodot, and nanodisk geometries, which agrees well with existing experimental results and first principles calculations. The simulation also shows that the nanoparticle favors c domains in the wire or rod geometries, a_1/a_2 domains and c domains in the nanodot geometry, and a_1/a_2 domains in the disk or film geometries. Simulated domain switching shows that with the shape of the nanoparticle changing from wire to film the coercive field, the saturated polarization, and the remnant polarization decrease under an externally applied electric field along the x_3 -direction.

Acknowledgements

This work was partially sponsored by the Project-Based Personnel Exchange Program of the China Scholarship Council and American Academic Exchange Service

[2008(3012)] and partially supported by the National Science Foundation of China under Grants nos. 11174030 and 51221291, 11202156 and the US National Science Foundation under Grant DMR-1006541. The computations were performed in the University of Science and Technology, Beijing, People's Republic of China and partially using the Cyberstar cluster at the Pennsylvania State University, funded by the National Science Foundation through Grant OCI-0821527.

Appendix A

The mechanical equilibrium equations must be solved to obtain the displacement and stress distributions in materials with arbitrary elastic inhomogeneity and anisotropy. We write the total elastic constant tensor as the sum of a homogeneous part c_{ijkl}^0 and an inhomogeneous perturbation $\Delta c_{ijkl}(\mathbf{r})$, i.e.

$$c_{ijkl}(\mathbf{r}) = c_{ijkl}^0 + \Delta c_{ijkl}(\mathbf{r}). \quad (\text{A1})$$

Let $\varepsilon_{ij}(\mathbf{r})$ denote the total strain measured with respect to a reference undeformed lattice. Then the local stress $\sigma_{ij}(\mathbf{r})$ is given as:

$$\sigma_{ij}(\mathbf{r}) = (c_{ijkl}^0 + \Delta c_{ijkl}(\mathbf{r}))(\varepsilon_{kl}(\mathbf{r}) - \varepsilon_{kl}^0(\mathbf{r})), \quad (\text{A2})$$

where $\varepsilon_{kl}^0(\mathbf{r})$ is the eigenstrain or stress-free strain. The mechanical equilibrium equation $\partial\sigma_{ij}(\mathbf{r})/\partial x_j = 0$ in an equilibrium system has to be satisfied, i.e.

$$\frac{\partial}{\partial x_j} [(c_{ijkl}^0 + \Delta c_{ijkl}(\mathbf{r}))(\varepsilon_{kl}(\mathbf{r}) - \varepsilon_{kl}^0(\mathbf{r}))] = 0. \quad (\text{A3})$$

According to Khachaturyan's elastic theory the total strain $\varepsilon_{ij}(\mathbf{r})$ may be expressed as the sum of homogeneous and heterogeneous strains[27], i.e.

$$\varepsilon_{ij}(\mathbf{r}) = \bar{\varepsilon}_{ij} + \delta\varepsilon_{ij}(\mathbf{r}), \quad (\text{A4})$$

where the homogeneous strain is defined in such a way that $\int \delta\varepsilon_{ij}(\mathbf{r})dV = 0$, and the homogeneous strain represents the macroscopic shape change of a system generated due to the formation of a domain structure. The heterogeneous strain doesn't change the macroscopic shape of a system, and it can be determined as

$$\delta\varepsilon_{ij}(\mathbf{r}) = \frac{1}{2} \left(\frac{\partial u_i(\mathbf{r})}{\partial x_j} + \frac{\partial u_j(\mathbf{r})}{\partial x_i} \right), \quad (\text{A5})$$

where $u_i(\mathbf{r})$ is the position-dependent displacement. Substituting Eqs. (A4) and (A5) into Eq. (A3) we obtain, after rearranging and simplifying,

$$c_{ijkl}^0 \frac{\partial^2 u_k(\mathbf{r})}{\partial x_j \partial x_l} = \frac{\partial}{\partial x_j} [(c_{ijkl}^0 + \Delta c_{ijkl}(\mathbf{r}))(\varepsilon_{kl}^0(\mathbf{r}) - \bar{\varepsilon}_{kl})] - \frac{\partial}{\partial x_j} \left[\Delta c_{ijkl}(\mathbf{r}) \frac{\partial u_k(\mathbf{r})}{\partial x_l} \right]. \quad (\text{A6})$$

For a zero order approximation where the elastic constants are assumed to be homogeneous one can solve Eq. (A6) by the Fourier spectral method. Thus Eq. (A6) becomes:

$$c_{ijkl}^0 \frac{\partial^2 u_k^0(\mathbf{r})}{\partial x_j \partial x_l} = c_{ijkl}^0 \frac{\partial \varepsilon_{kl}^0(\mathbf{r})}{\partial x_j}. \quad (\text{A7})$$

By applying Fourier transforms to Eq. (A7) we obtain:

$$-c_{ijkl}^0 q_j q_l \tilde{u}_k^0(\mathbf{q}) = I q_j c_{ijkl}^0 \tilde{\varepsilon}_{kl}^0(\mathbf{q}), \quad (\text{A8})$$

where $\tilde{u}_k^0(\mathbf{q})$ and $\tilde{\varepsilon}_{kl}^0(\mathbf{q})$ are Fourier transforms of $u_k^0(\mathbf{r})$ and $\varepsilon_{kl}^0(\mathbf{r})$, $\tilde{u}_k^0(\mathbf{q}) = \int_V u_k^0(\mathbf{r}) e^{-i\mathbf{q}\cdot\mathbf{r}} d^3r$, and $\tilde{\varepsilon}_{kl}^0(\mathbf{q}) = \int_V \varepsilon_{kl}^0(\mathbf{r}) e^{-i\mathbf{q}\cdot\mathbf{r}} d^3r$, respectively, \mathbf{q} is the reciprocal lattice vector, q_j is the j th component of \mathbf{q} , and I is the imaginary unit. Solving for displacement we get:

$$\tilde{u}_k^0(\mathbf{q}) = -I q_j G_{ik}(\mathbf{q}) c_{ijkl}^0 \tilde{\varepsilon}_{kl}^0(\mathbf{q}), \quad (\text{A9})$$

where $G_{ik}(\mathbf{q})$ is the Green tensor whose inverse is defined as $G_{ik}^{-1}(\mathbf{q}) = c_{ijkl}^0 q_j q_l$. After taking the inverse Fourier transforms on both sides of Eq. (A9) we obtain the zero order approximation of the displacement:

$$u_k^0(\mathbf{r}) = - \int \frac{d^3q}{(2\pi)^3} I q_j G_{ik}(\mathbf{q}) c_{ijkl}^0 \tilde{\varepsilon}_{kl}^0(\mathbf{q}) e^{i\mathbf{q}\cdot\mathbf{r}}. \quad (\text{A10})$$

Substituting the zero order displacement (Eq. (A10)) in the iterative Eq. (A6) we obtain the first order displacement iteration:

$$c_{ijkl}^0 \frac{\partial^2 u_k^1(\mathbf{r})}{\partial x_j \partial x_l} = \frac{\partial}{\partial x_j} [(c_{ijkl}^0 + \Delta c_{ijkl}(\mathbf{r}))(\varepsilon_{kl}^0(\mathbf{r}) - \bar{\varepsilon}_{kl})] - \frac{\partial}{\partial x_j} \left[\Delta c_{ijkl}(\mathbf{r}) \frac{\partial u_k^0(\mathbf{r})}{\partial x_l} \right]. \quad (\text{A11})$$

The solution of $u_k^1(\mathbf{r})$ is obtained in Fourier space:

$$\tilde{u}_k^1(\mathbf{q}) = -I G_{ik}(\mathbf{q}) q_j \left\{ (c_{ijkl}^0 + \Delta c_{ijkl}(\mathbf{r}))(\varepsilon_{kl}^0(\mathbf{r}) - \bar{\varepsilon}_{kl}) - \Delta c_{ijkl}(\mathbf{r}) \frac{\partial u_k^0(\mathbf{r})}{\partial x_l} \right\}_{\mathbf{q}}, \quad (\text{A12})$$

where $\left\{ (c_{ijkl}^0 + \Delta c_{ijkl}(\mathbf{r}))(\varepsilon_{kl}^0(\mathbf{r}) - \bar{\varepsilon}_{kl}) - \Delta c_{ijkl}(\mathbf{r}) \frac{\partial u_k^0(\mathbf{r})}{\partial x_l} \right\}_{\mathbf{q}}$ indicates the Fourier transforms of $(c_{ijkl}^0 + \Delta c_{ijkl}(\mathbf{r}))(\varepsilon_{kl}^0(\mathbf{r}) - \bar{\varepsilon}_{kl}) - \Delta c_{ijkl}(\mathbf{r}) \frac{\partial u_k^0(\mathbf{r})}{\partial x_l}$. The higher order solutions for $u_k(\mathbf{r})$ are derived in a similar way to the first order approximation:

$$c_{ijkl}^0 \frac{\partial^2 u_k^n(\mathbf{r})}{\partial x_j \partial x_l} = \frac{\partial}{\partial x_j} [(c_{ijkl}^0 + \Delta c_{ijkl}(\mathbf{r}))(\varepsilon_{kl}^0(\mathbf{r}) - \bar{\varepsilon}_{kl})] - \frac{\partial}{\partial x_j} \left[\Delta c_{ijkl}(\mathbf{r}) \frac{\partial u_k^{n-1}(\mathbf{r})}{\partial x_l} \right]. \quad (\text{A13})$$

As with $u_k^1(\mathbf{r})$, the solution for $u_k^n(\mathbf{r})$ is solved using Fourier transforms:

$$\tilde{u}_k^n(\mathbf{q}) = -I G_{ik}(\mathbf{q}) q_j \left\{ (c_{ijkl}^0 + \Delta c_{ijkl}(\mathbf{r}))(\varepsilon_{kl}^0(\mathbf{r}) - \bar{\varepsilon}_{kl}) - \Delta c_{ijkl}(\mathbf{r}) \frac{\partial u_k^{n-1}(\mathbf{r})}{\partial x_l} \right\}_{\mathbf{q}}. \quad (\text{A14})$$

The homogeneous strain is determined by the mechanical boundary conditions for the system. When the system is under a constant strain $\varepsilon_{kl}^{\text{app}}$ the homogeneous strain $\bar{\varepsilon}_{kl}$ is equal to the applied strain, i.e. $\bar{\varepsilon}_{kl} = \varepsilon_{kl}^{\text{app}}$. However, when the boundaries of the system are allowed to relax (or a specified stressed boundary condition is applied) the homogeneous strain is obtained by minimizing the total elastic energy. When the system is subjected to an applied stress

σ_{kl}^{app} the total elastic energy of the system is written as [60,61]:

$$F_{\text{el}} = \frac{1}{2} \int_V c_{ijkl}(\mathbf{r}) [\bar{\varepsilon}_{ij} + \delta\varepsilon_{ij}(\mathbf{r}) - \varepsilon_{ij}^0(\mathbf{r})] [\bar{\varepsilon}_{kl} + \delta\varepsilon_{kl}(\mathbf{r}) - \varepsilon_{kl}^0(\mathbf{r})] dV. \quad (\text{A15})$$

Minimization of the total elastic energy with respect to the homogeneous strain yields:

$$\bar{\varepsilon}_{kl} = \langle s_{ijkl}(\mathbf{r}) \rangle \left(\sigma_{ij}^{\text{app}} + \langle \sigma_{ij}^0(\mathbf{r}) \rangle - \langle \delta\sigma_{ij}(\mathbf{r}) \rangle \right), \quad (\text{A16})$$

where $\langle s_{ijkl}(\mathbf{r}) \rangle = \langle c_{ijkl}(\mathbf{r}) \rangle^{-1}$, $\langle c_{ijkl}(\mathbf{r}) \rangle = (1/V) \int_V c_{ijkl}(\mathbf{r}) dV$, $\langle \sigma_{ij}^0(\mathbf{r}) \rangle = (1/V) \int_V c_{ijkl}(\mathbf{r}) \varepsilon_{kl}^0(\mathbf{r}) dV$, and $\langle \delta\sigma_{ij}(\mathbf{r}) \rangle = (1/V) \int_V c_{ijkl}(\mathbf{r}) \delta\varepsilon_{kl}(\mathbf{r}) dV$.

References

- [1] Ahn CH, Rabe KM, Triscone JM. *Science* 2004;303:488.
- [2] Scott JF, Dearaujo CAP. *Science* 1989;246:1400.
- [3] Scott JF. *Science* 2007;315:954.
- [4] Evans PR, Zhu XH, Baxter P, McMillen M, McPhillips J, Morrison FD, et al. *Nano Lett* 2007;7:1134.
- [5] Naumov II, Bellaiche L, Fu H. *Nature* 2004;432:737.
- [6] Liu JF, Li XL, Li YD. *J Nanosci Nanotechnol* 2002;2:617.
- [7] Urban JJ, Yun WS, Gu Q, Park H. *J Am Chem Soc* 2002;124:1186.
- [8] Yun WS, Urban JJ, Gu Q, Park H. *Nano Lett* 2002;2:447.
- [9] Luo Y, Szafraniak I, Zakharov ND, Nagarajan V, Steinhart M, Wehrspohn RB, et al. *Appl Phys Lett* 2003;83:440.
- [10] Mao YB, Banerjee S, Wong SS. *J Am Chem Soc* 2003;125:15718.
- [11] Alexe M, Hesse D, Schmidt V, Senz S, Fan HJ, Zacharias M, et al. *Appl Phys Lett* 2006;89:172907.
- [12] Spanier JE, Kolpak AM, Urban JJ, Grinberg I, Lian OY, Yun WS, et al. *Nano Lett* 2006;6:735.
- [13] Morozovska AN, Eliseev EA, Glinchuk MD. *Phys Rev B* 2006;73:214106.
- [14] Wang JJ, Eliseev EA, Ma XQ, Wu PP, Morozovska AN, Chen LQ. *Acta Mater* 2011;59:7189.
- [15] Leo PH, Lowengrub JS, Jou HJ. *Acta Mater* 1998;46:2113.
- [16] Zhu JZ, Chen LQ, Shen J. *Modell Simul Mater Sci Eng* 2001;9:499.
- [17] Wang YU, Jin YM, Khachaturyan AG. *Appl Phys Lett* 2002;80:4513.
- [18] Wang YU, Jin YMM, Khachaturyan AG. *J Appl Phys* 2002;92:1351.
- [19] Hu SY, Chen LQ. *Acta Mater* 2001;49:1879.
- [20] Wang JJ, Bhattacharyya S, Li Q, Heo TW, Ma XQ, Chen LQ. *Philos Mag Lett* 2012;92:327.
- [21] Wang B, Woo CH. *J Appl Phys* 2005;97:084109.
- [22] Wang B, Woo CH. *J Appl Phys* 2006;100:044114.
- [23] Woo CH, Zheng Y. *Appl Phys A Mater Sci Process* 2008;91:59.
- [24] Li YL, Hu SY, Liu ZK, Chen LQ. *Appl Phys Lett* 2002;81:427.
- [25] Tagantsev A. *Ferroelectrics* 1986;69:321.
- [26] Fu H, Bellaiche L. *Phys Rev Lett* 2003;91:257601.
- [27] Khachaturyan AG. *Theory of structural transformations in solids*. New York: Wiley; 1983.
- [28] Bhattacharyya S, Heo TW, Chang K, Chen LQ. *Modell Simul Mater Sci Eng* 2011;19:035002.
- [29] Ma W, Zhang M, Lu Z. *Phys Status Solidi A* 1998;166:811.
- [30] Uchino K, Sadanaga E, Hirose T. *J Am Ceram Soc* 1989;72:1555.
- [31] Ma W. *Appl Phys A Mater Sci Process* 2009;96:915.
- [32] Wu P, Ma X, Li Y, Gopalan V, Chen L-Q. *Appl Phys Lett* 2012;100:092905.
- [33] Tagantsev AK. *Ferroelectrics* 2008;375:19.
- [34] Kittel C. *Introduction to solid state physics*. New York: Wiley; 1996.
- [35] Semenovskaya S, Khachaturyan A. *J Appl Phys* 1998;83:5125.
- [36] Wang YU. *Appl Phys Lett* 2010;96:232901.
- [37] C. Paz de Araujo, J.F. Scott, G.F. Taylor, in: D.R. Tilley (Ed.), *Ferroelectric thin films: synthesis and basic properties*, Gordon & Breach, New York.
- [38] Wang CL, Smith SRP. *J Phys: Condens Matter* 1999;7:7163.
- [39] Hong L, Soh A, Song Y, Lim L. *Acta Mater* 2008;56:2966.
- [40] Lo VC. *J Appl Phys* 2003;94:3353.
- [41] Haun MJ, Furman E, Halemane TR, Cross LE. *Ferroelectrics* 1989;99:55.
- [42] Haun MJ, Furman E, Jang SJ, Cross LE. *Ferroelectrics* 1989;99:13.
- [43] Haun MJ, Furman E, Jang SJ, Cross LE. *Ferroelectrics* 1989;99:63.
- [44] Haun MJ, Furman E, McKinstry HA, Cross LE. *Ferroelectrics* 1989;99:27.
- [45] Haun MJ, Zhuang ZQ, Furman E, Jang SJ, Cross LE. *Ferroelectrics* 1989;99:45.
- [46] Li YL, Choudhury S, Liu ZK, Chen LQ. *Appl Phys Lett* 2003;83:1608.
- [47] Yadlovker D, Berger S. *Phys Rev B* 2005;71:184112.
- [48] Pertsev NA, Zembilgotov AG, Tagantsev AK. *Phys Rev Lett* 1998;80:1988.
- [49] Li YL, Chen LQ. *Appl Phys Lett* 2006;88:072905.
- [50] Naumov II, Fu H. *Phys Rev Lett* 2005;95:247602.
- [51] Streiffer SKt, Eastman JA, Fong DD, Thompson C, Munkholm A, Ramana Murty MV, et al. *Phys Rev Lett* 2002;89:67601.
- [52] Ishikawa K, Yoshikawa K, Okada N. *Phys Rev B* 1988;37:5852.
- [53] Ishikawa K, Nomura T, Okada N, Takada K. *Jpn J Appl Phys* 1996;35:5196.
- [54] Zhong WL, Jiang B, Zhang PL, Ma JM, Cheng HM, Yang ZH. *J Phys: Condens Matter* 1999;5:2619.
- [55] Wang JJ, Wu PP, Ma XQ, Chen LQ. *J Appl Phys* 2010;108:114105.
- [56] Slutsker J, Artemev A, Roytburd A. *Phys Rev Lett* 2008;100:87602.
- [57] Wang J, Kamlah M, Zhang T-Y, Li Y, Chen L-Q. *Appl Phys Lett* 2008;92:162905.
- [58] Schilling A, Byrne D, Catalan G, Webber KG, Genenko YA, Wu GS, et al. *Nano Lett* 2009;9:3359.
- [59] Prosandeev S, Bellaiche L. *Phys Rev B* 2007;75:094102.
- [60] Li DY, Chen LQ. *Acta Mater* 1998;47:247.
- [61] Bhattacharyya S, Heo TW, Chang K, Chen LQ. *Commun Comput Phys* 2012;11:726.